

PAPER

First cryogenic test operation of underground km-scale gravitational-wave observatory KAGRA

To cite this article: T Akutsu *et al* 2019 *Class. Quantum Grav.* **36** 165008

View the [article online](#) for updates and enhancements.

Recent citations

- [Thermal noise and mechanical loss of SiO₂/Ta₂O₅ optical coatings at cryogenic temperatures](#)
John M. Robinson *et al*
- [The Hunt for Environmental Noise in Virgo during the Third Observing Run](#)
Irene Fiori *et al*
- [Overview of KAGRA: Detector design and construction history](#)
T Akutsu *et al*



IOP ebooks™

Bringing together innovative digital publishing with leading authors from the global scientific community.

Start exploring the collection—download the first chapter of every title for free.

First cryogenic test operation of underground km-scale gravitational-wave observatory KAGRA

T Akutsu^{1,2}, M Ando^{1,3,4}, K Arai⁵, Y Arai⁵, S Araki⁶,
A Araya⁷, N Aritomi³, H Asada⁸, Y Aso^{9,10}, S Atsuta¹¹,
K Awai¹², S Bae¹³, L Baiotti¹⁴, M A Barton¹, K Cannon⁴,
E Capocasa¹, C-S Chen¹⁵, T-W Chiu¹⁵, K Cho¹⁶, Y-
K Chu¹⁵, K Craig⁵, W Creus¹⁷, K Doi¹⁸, K Eda⁴, Y Enomoto³,
R Flaminio^{1,19}, Y Fujii²⁰, M-K Fujimoto¹, M Fukunaga⁵,
M Fukushima², T Furuhata¹⁸, A Hagiwara²¹, S Haino¹⁷,
K Hasegawa⁵, K Hashino¹⁸, K Hayama²², S Hirobayashi²³,
E Hirose⁵, B H Hsieh²⁴, C-Z Huang¹⁵, B Ikenoue²,
Y Inoue^{21,25,26}, K Ioka²⁷, Y Itoh²⁸, K Izumi²⁹, T Kaji²⁸,
T Kajita³⁰, M Kakizaki¹⁸, M Kamiizumi¹², S Kanbara¹⁸,
N Kanda²⁸, S Kanemura¹⁴, M Kaneyama²⁸, G Kang¹³,
J Kasuya¹¹, Y Kataoka¹¹, N Kawai¹¹, S Kawamura¹²,
T Kawasaki³, C Kim³¹, J Kim³², J C Kim³³, W S Kim³⁴,
Y-M Kim³⁵, N Kimura²¹, T Kinugawa⁵, S Kirii¹², Y Kitaoka²⁸,
H Kitazawa¹⁸, Y Kojima³⁶, K Kokeyama¹², K Komori³,
A K H Kong³⁷, K Kotake²², R Kozu³⁸, R Kumar³⁹,
H-S Kuo¹⁵, S Kuroyanagi⁴⁰, H K Lee⁴¹, H M Lee⁴²,
H W Lee³³, M Leonardi¹, C-Y Lin⁴³, F-L Lin^{4,15}, G C Liu⁴⁴,
Y Liu⁴⁵, E Majorana⁴⁶, S Mano⁴⁷, M Marchio¹, T Matsui⁴⁸,
F Matsushima¹⁸, Y Michimura³, N Mio⁴⁹, O Miyakawa¹²,
A Miyamoto²⁸, T Miyamoto³⁸, K Miyo¹², S Miyoki¹², W Morii⁵⁰,
S Morisaki⁴, Y Moriwaki¹⁸, T Morozumi⁵, I Murakami²¹,
M Musha⁵¹, K Nagano⁵, S Nagano⁵², K Nakamura¹,
T Nakamura⁵³, H Nakano⁵⁴, M Nakano⁵, K Nakao²⁸,
Y Namai²¹, T Narikawa⁵³, L Naticchioni⁴⁶,
L Nguyen Quynh⁵⁵, W-T Ni^{37,56,57}, A Nishizawa⁴⁰, Y Obuchi²,
T Ochi⁵, J J Oh³⁴, S H Oh³⁴, M Ohashi¹², N Ohishi⁹,
M Ohkawa⁵⁸, K Okutomi¹⁰, K Ono⁵, K Oohara⁵⁹, C P Ooi³,
S-S Pan⁶⁰, J Park¹⁶, F E Peña Arellano¹², I Pinto⁶¹,
N Sago⁶², M Saijo⁶³, Y Saito¹², S Saitou², K Sakai⁶⁴,
Y Sakai⁵⁹, Y Sakai³, M Sasai²⁸, M Sasaki⁶⁵, Y Sasaki⁶⁶,
N Sato², S Sato⁶⁷, T Sato⁵⁸, Y Sekiguchi⁶⁸, N Seto⁵³,
M Shibata²⁷, T Shimoda³, H Shinkai⁶⁹, T Shishido⁷⁰,
A Shoda¹, K Somiya¹¹, E J Son³⁴, A Suemasa⁵¹,

**T Suzuki⁵⁸, T Suzuki⁵, H Tagoshi⁵, H Tahara²⁰, H Takahashi⁶⁶,
 R Takahashi¹, A Takamori⁷, H Takeda³, H Tanaka²⁴,
 K Tanaka²⁸, T Tanaka⁵³, S Tanioka^{1,10} , E N Tapia San
 Martin¹, D Tatsumi¹, S Terashima²¹, T Tomaru²¹, T Tomura¹²,
 F Travasso⁷¹ , K Tsubono³, S Tsuchida²⁸, N Uchikata⁷²,
 T Uchiyama¹², A Ueda²¹, T Uehara^{73,74} , S Ueki⁶⁶,
 K Ueno⁴, F Uraguchi², T Ushiba⁵, M H P M van Putten⁷⁵,
 H Vocca⁷¹ , S Wada³, T Wakamatsu⁵⁹, Y Watanabe⁵⁹,
 W-R Xu¹⁵, T Yamada²⁴, A Yamamoto⁶, K Yamamoto¹⁸,
 K Yamamoto²⁴ , S Yamamoto⁶⁹, T Yamamoto¹² ,
 K Yokogawa¹⁸, J Yokoyama^{3,4,20}, T Yokozawa¹², T H Yoon⁷⁶,
 T Yoshioka¹⁸, H Yuzurihara⁵, S Zeidler¹ and Z-H Zhu⁷⁷ **
(The KAGRA Collaboration)

¹ National Astronomical Observatory of Japan (NAOJ), Mitaka City, Tokyo 181-8588, Japan

² Advanced Technology Center, National Astronomical Observatory of Japan (NAOJ), Mitaka City, Tokyo 181-8588, Japan

³ Department of Physics, The University of Tokyo, Bunkyo-ku, Tokyo 113-0033, Japan

⁴ Research Center for the Early Universe (RESCEU), The University of Tokyo, Bunkyo-ku, Tokyo 113-0033, Japan

⁵ Institute for Cosmic Ray Research (ICRR), KAGRA Observatory, The University of Tokyo, Kashiwa City, Chiba 277-8582, Japan

⁶ Accelerator Laboratory, High Energy Accelerator Research Organization (KEK), Tsukuba City, Ibaraki 305-0801, Japan

⁷ Earthquake Research Institute, The University of Tokyo, Bunkyo-ku, Tokyo 113-0032, Japan

⁸ Department of Mathematics and Physics, Hirosaki University, Hirosaki City, Aomori 036-8561, Japan

⁹ Kamioka Branch, National Astronomical Observatory of Japan (NAOJ), Kamioka-cho, Hida City, Gifu 506-1205, Japan

¹⁰ The Graduate University for Advanced Studies (SOKENDAI), Mitaka City, Tokyo 181-8588, Japan

¹¹ Graduate School of Science and Technology, Tokyo Institute of Technology, Meguro-ku, Tokyo 152-8551, Japan

¹² Institute for Cosmic Ray Research (ICRR), KAGRA Observatory, The University of Tokyo, Kamioka-cho, Hida City, Gifu 506-1205, Japan

¹³ Korea Institute of Science and Technology Information (KISTI), Yuseong-gu, Daejeon 34141, Republic of Korea

¹⁴ Graduate School of Science, Osaka University, Toyonaka City, Osaka 560-0043, Japan

¹⁵ Department of Physics, National Taiwan Normal University, sec. 4, Taipei 116, Taiwan, Republic of China

¹⁶ Department of Physics, Sogang University, Mapo-Gu, Seoul 121-742, Republic of Korea

¹⁷ Institute of Physics, Academia Sinica, Nankang, Taipei 11529, Taiwan, Republic of China

¹⁸ Department of Physics, University of Toyama, Toyama City, Toyama 930-8555, Japan

¹⁹ Laboratoire d'Annecy de Physique des Particules (LAPP), Univ. Grenoble Alpes, Université Savoie Mont Blanc, CNRS/IN2P3, F-74941 Annecy, France

- ²⁰ Department of Astronomy, The University of Tokyo, Bunkyo-ku, Tokyo 113-0033, Japan
- ²¹ Applied Research Laboratory, High Energy Accelerator Research Organization (KEK), Tsukuba City, Ibaraki 305-0801, Japan
- ²² Department of Applied Physics, Fukuoka University, Jonan, Fukuoka City, Fukuoka 814-0180, Japan
- ²³ Faculty of Engineering, University of Toyama, Toyama City, Toyama 930-8555, Japan
- ²⁴ Institute for Cosmic Ray Research (ICRR), Research Center for Cosmic Neutrinos (RCCN), The University of Tokyo, Kashiwa City, Chiba 277-8582, Japan
- ²⁵ Department of Physics, National Central University, Zhongli District, Taoyuan City 32001, Taiwan, Republic of China
- ²⁶ Center for High Energy and High Field Physics, Zhongli District, Taoyuan City 32001, Taiwan, Republic of China
- ²⁷ Yukawa Institute for Theoretical Physics (YITP), Kyoto University, Sakyo-ku, Kyoto City, Kyoto 606-8502, Japan
- ²⁸ Graduate School of Science, Osaka City University, Sumiyoshi-ku, Osaka City, Osaka 558-8585, Japan
- ²⁹ JAXA Institute of Space and Astronautical Science, Chuo-ku, Sagami-hara City, Kanagawa 252-0222, Japan
- ³⁰ Institute for Cosmic Ray Research (ICRR), The University of Tokyo, Kashiwa City, Chiba 277-8582, Japan
- ³¹ Department of Physics, Ewha Womans University, Seodaemun-gu, Seoul 03760, Republic of Korea
- ³² Department of Physics, Myongji University, Yongin 449-728, Republic of Korea
- ³³ Department of Computer Simulation, Inje University, Gimhae, Gyeongsangnam-do 50834, Republic of Korea
- ³⁴ National Institute for Mathematical Sciences, Daejeon 34047, Republic of Korea
- ³⁵ School of Natural Science, Ulsan National Institute of Science and Technology (UNIST), Ulsan 44919, Republic of Korea
- ³⁶ Department of Physical Science, Hiroshima University, Higashihiroshima City, Hiroshima 903-0213, Japan
- ³⁷ Department of Physics and Institute of Astronomy, National Tsing Hua University, Hsinchu 30013, Taiwan, Republic of China
- ³⁸ Institute for Cosmic Ray Research (ICRR), Research Center for Cosmic Neutrinos (RCCN), The University of Tokyo, Kamioka-cho, Gifu City, Gifu 506-1205, Japan
- ³⁹ California Institute of Technology, Pasadena, CA 91125, United States of America
- ⁴⁰ Institute for Advanced Research, Nagoya University, Furocho, Chikusa-ku, Nagoya City, Aichi 464-8602, Japan
- ⁴¹ Department of Physics, Hanyang University, Seoul 133-791, Republic of Korea
- ⁴² Korea Astronomy and Space Science Institute (KASI), Yuseong-gu, Daejeon 34055, Republic of Korea
- ⁴³ National Center for High-performance computing, National Applied Research Laboratories, Hsinchu Science Park, Hsinchu City 30076, Taiwan, Republic of China
- ⁴⁴ Department of Physics, Tamkang University, Danshui Dist., New Taipei City 25137, Taiwan, Republic of China
- ⁴⁵ Department of Advanced Materials Science, The University of Tokyo, Kashiwa City, Chiba 277-8582, Japan
- ⁴⁶ Istituto Nazionale di Fisica Nucleare, Sapienza University, Roma 00185, Italy
- ⁴⁷ Department of Mathematical Analysis and Statistical Inference, The Institute of Statistical Mathematics, Tachikawa City, Tokyo 190-8562, Japan
- ⁴⁸ School of Physics, Korea Institute for Advanced Study (KIAS), Seoul 02455, Republic of Korea

- ⁴⁹ Institute for Photon Science and Technology, The University of Tokyo, Bunkyo-ku, Tokyo 113-8656, Japan
- ⁵⁰ Disaster Prevention Research Institute, Kyoto University, Uji City, Kyoto 611-0011, Japan
- ⁵¹ Institute for Laser Science, University of Electro-Communications, Chofu City, Tokyo 182-8585, Japan
- ⁵² The Applied Electromagnetic Research Institute, National Institute of Information and Communications Technology (NICT), Koganei City, Tokyo 184-8795, Japan
- ⁵³ Department of Physics, Kyoto University, Sakyou-ku, Kyoto City, Kyoto 606-8502, Japan
- ⁵⁴ Faculty of Law, Ryukoku University, Fushimi-ku, Kyoto City, Kyoto 612-8577, Japan
- ⁵⁵ Department of Physics, University of Notre Dame, Notre Dame, IN 46556, United States of America
- ⁵⁶ Department of Physics, Wuhan Institute of Physics and Mathematics, CAS, Xiaohongshan, Wuhan 430071, People's Republic of China
- ⁵⁷ School of Optical Electrical and Computer Engineering, The University of Shanghai for Science and Technology, Shanghai 200093, People's Republic of China
- ⁵⁸ Faculty of Engineering, Niigata University, Nishi-ku, Niigata City, Niigata 950-2181, Japan
- ⁵⁹ Graduate School of Science and Technology, Niigata University, Nishi-ku, Niigata City, Niigata 950-2181, Japan
- ⁶⁰ Center for Measurement Standards, Industrial Technology Research Institute, Hsinchu, 30011, Taiwan, Republic of China
- ⁶¹ Department of Engineering, University of Sannio, Benevento 82100, Italy
- ⁶² Faculty of Arts and Science, Kyushu University, Nishi-ku, Fukuoka City, Fukuoka 819-0395, Japan
- ⁶³ Research Institute for Science and Engineering, Waseda University, Shinjuku, Tokyo 169-8555, Japan
- ⁶⁴ Department of Electronic Control Engineering, National Institute of Technology, Nagaoka College, Nagaoka City, Niigata 940-8532, Japan
- ⁶⁵ Kavli Institute for the Physics and Mathematics of the Universe (IPMU), Kashiwa City, Chiba 277-8583, Japan
- ⁶⁶ Department of Information & Management Systems Engineering, Nagaoka University of Technology, Nagaoka City, Niigata 940-2188, Japan
- ⁶⁷ Graduate School of Science and Engineering, Hosei University, Koganei City, Tokyo 184-8584, Japan
- ⁶⁸ Faculty of Science, Toho University, Funabashi City, Chiba 274-8510, Japan
- ⁶⁹ Faculty of Information Science and Technology, Osaka Institute of Technology, Hirakata City, Osaka 573-0196, Japan
- ⁷⁰ School of High Energy Accelerator Science, The Graduate University for Advanced Studies (SOKENDAI), Tsukuba City, Ibaraki 305-0801, Japan
- ⁷¹ Istituto Nazionale di Fisica Nucleare, University of Perugia, Perugia 06123, Italy
- ⁷² Faculty of Science, Niigata University, Nishi-ku, Niigata City, Niigata 950-2181, Japan
- ⁷³ Department of Communications, National Defense Academy of Japan, Yokosuka City, Kanagawa 239-8686, Japan
- ⁷⁴ Department of Physics, University of Florida, Gainesville, FL 32611, United States of America
- ⁷⁵ Department of Physics and Astronomy, Sejong University, Gwangjin-gu, Seoul 143-747, Republic of Korea
- ⁷⁶ Department of Physics, Korea University, Seongbuk-gu, Seoul 02841, Republic of Korea

⁷⁷ Department of Astronomy, Beijing Normal University, Beijing 100875, People's Republic of China

E-mail: Sadakazu.Haino@cern.ch, kanda@sci.osaka-cu.ac.jp,
michimura@granite.phys.s.u-tokyo.ac.jp, hisaaki.shinkai@oit.ac.jp
and yamat@icrr.u-tokyo.ac.jp

Received 11 January 2019, revised 12 April 2019
Accepted for publication 11 June 2019
Published 23 July 2019



CrossMark

Abstract

KAGRA is a second-generation interferometric gravitational-wave detector with 3 km arms constructed at Kamioka, Gifu, Japan. It is now in its final installation phase, which we call *bKAGRA* (baseline KAGRA), with scientific observations expected to begin in late 2019. One of the advantages of KAGRA is its underground location of at least 200 m below the ground surface, which reduces seismic motion at low frequencies and increases the stability of the detector. Another advantage is that it cools down the sapphire test mass mirrors to cryogenic temperatures to reduce thermal noise. In April–May 2018, we operated a 3 km Michelson interferometer with a cryogenic test mass for 10 d, which was the first time that km-scale interferometer was operated at cryogenic temperatures. In this article, we report the results of this ‘bKAGRA Phase 1’ operation. We have demonstrated the feasibility of 3 km interferometer alignment and control with cryogenic mirrors.

Keywords: gravitational waves, cryogenic laser interferometer, sapphire, underground

(Some figures may appear in colour only in the online journal)

1. Introduction

Direct detection of gravitational waves (GWs) in the past three years have proved that we are entering a new era of physics and astronomy. The LIGO Scientific Collaboration and Virgo Collaboration have so far reported ten binary black hole mergers (GW150914 [1], and others [2]), and one binary neutron star merger (GW170817 [3]) during their first and second observing runs (O1 and O2). According to the latest release [2], the sources of GWs vary in distance from 320_{-110}^{+120} Mpc to 2750_{-1320}^{+1350} Mpc and total-mass for the black hole binaries range from $18.6_{-0.7}^{+3.1} M_{\odot}$ to $85.1_{-10.9}^{+15.6} M_{\odot}$. LIGO and Virgo also list fourteen additional marginal events [4]. These numbers tell us that hunting for GWs is now a part of astronomy, that is, we now have a totally new set of ‘eyes’ to observe the Universe.

Information from GWs enables us not only to identify the parameters of compact objects, but to also model and provide constraints of many physical and astrophysical phenomena. As for the neutron-star binary merger (GW170817), after the short notice of the detection by LIGO and Virgo, successive observations of the source using γ -ray, x-ray, UV, optical, IR, and radio telescopes were made. These observations identified the source, and revealed the nature of the gigantic astrophysical event; details such as the plausible evidence of a rapid process of nuclear fusion, constraints to equation of state of nuclear matter, constraints to cosmological

models, and so on. In the near future, we are quite certain that strong gravitational effects from black holes will provide us a chance to test Einstein's general relativity. Accumulation of detections will also allow us to discuss the formation processes of stars and binaries.

The LIGO Scientific Collaboration has two 4 km arm laser interferometers at Hanford, Washington state, and at Livingston, Louisiana state [5]. The independent detection from these two detectors provided the first 5 detections of GWs. The Virgo Collaboration has a 3 km arm laser interferometer at Pisa, Italy [6], and its joint observation with LIGO in August 2017 resulted in detection with high precision in its source localization, which significantly aided the follow-up electromagnetic observation of the source by astronomers. In principle, GWs should be detected independently at different locations in order to rule out false positives. If three detectors are operating simultaneously, we are able to identify the location of the source. With more detectors, we will get more precise information of parameters, including the polarization of GWs. With this in mind, KAGRA is the next interferometer joining to the GW network.

KAGRA is a 3 km laser interferometer, constructed in Kamioka, Gifu, Japan, and is now in its final installation phase [7, 8]⁷⁸. KAGRA is operated at cryogenic temperatures to reduce thermal noise around the detector's most sensitive band at around 100 Hz, and located at underground for smaller seismic noise. The future GW detector concepts such as Einstein Telescope [10] and Cosmic Explorer [11] consider to use these techniques, and therefore demonstrating the techniques with KAGRA is a key to the next generation GW detectors.

Since KAGRA is located far from both LIGO and Virgo, KAGRA's operation is expected to make the source localization and waveform reconstruction more precise, when all three observatories (LIGO, Virgo and KAGRA) perform the observation jointly [12]. Moreover, increasing the number of detectors is intrinsically essential to search for non-tensorial polarization modes of GWs to test general relativity [13, 14].

The KAGRA project is split into two stages, initial KAGRA (*iKAGRA*) and baseline KAGRA (*bKAGRA*), as summarized in table 1. In the *iKAGRA* stage, we had constructed the basic infrastructure including the tunnel and vacuum systems, and formed a simple 3 km Michelson interferometer that consisted of two end test masses and a beam splitter. The mirrors were fused silica mirrors at room temperature suspended by simplified systems. We operated *iKAGRA* in March and April of 2016, which was the first kilometer-scale interferometer operated underground. We first had to overcome challenges such as measuring the exact positions of the vacuum systems and the synchronization of digital real-time control systems 3 km apart in the tunnel using the Global Positioning System. In the *iKAGRA* operation, we demonstrated that the vacuum tubes are aligned well enough to form the interferometer, and real-time interferometer control was possible. For details of the *iKAGRA* operation, see [15].

The *bKAGRA* stage is focused on GW observations with a cryogenic resonant side-band extraction (RSE) interferometer. Before operating a full interferometer, we first constructed a 3 km Michelson interferometer with two sapphire test masses. All the mirrors were suspended by full systems, and one of the test masses was cooled down to cryogenic temperatures. This phase is called *bKAGRA Phase 1*, and we operated the interferometer from April 28 to May 6 in 2018. This operation was the first cryogenic operation with full suspension systems. The purpose of this article is to report the results of this operation. We characterized the suspensions and tested the compatibility of cryogenic cooling with 3-km interferometer alignment and control.

⁷⁸ KAGRA was originally called LCGT (large-scale cryogenic gravitational-wave telescope), but was renamed after the approval of the project via a public naming contest. The name KAGRA remind us of Kamioka (the location) plus gravity, and is also the Japanese word for traditional sacred music and dance in front of the gods. A detailed history of KAGRA is described in [9].

Table 1. Summary of the phases of KAGRA. Type-C suspension is a double pendulum and Type-A suspension is a full eight-stage pendulum (see section 2 for details). RSE: resonant sideband extraction interferometer.

	iKAGRA	bKAGRA phase 1	bKAGRA
Operation year	Mar-Apr 2016	Apr-May 2018	2019- (planned)
Interferometer configuration	3 km Michelson	3 km Michelson	3 km RSE
Test mass substrate	Fused silica	Sapphire	Sapphire
Test mass temperature	Room temp.	18 K/room temp.	22 K
Test mass suspension	Type-C	Type-A	Type-A

Table 2. List of acronyms used throughout this article.

BS	Beam splitter
ETMX (Y)	End test mass for X-arm (Y-arm)
GAS	Geometric anti-spring
GW	Gravitational wave
IMC	Input mode cleaner
ITMX (Y)	Input test mass for X-arm (Y-arm)
PRM	Power recycling mirror
RSE	Resonant sideband extraction
SRM	Signal recycling mirror

We start this article by describing the full configuration of bKAGRA in section 2. We then describe the details of bKAGRA Phase 1 operation and the results in section 3. Finally, we summarize the current status and our future prospects in section 4. Acronyms used throughout this article is summarized in table 2.

2. Interferometer configuration of bKAGRA

The schematic of the interferometer of bKAGRA is shown in figure 1. We use a single-frequency continuous-wave laser at a wavelength of 1064 nm. The main part of the interferometer is an RSE interferometer with two Fabry–Pérot arm cavities formed by input test masses (ITMs) and end test masses (ETMs) at 22 K [16]. Unlike the LIGO and Virgo detectors, we have chosen sapphire as the test mass material because of its high thermal conductivity and high Q value at cryogenic temperatures, which helps in both cooling and lowering thermal noise. We use 22.8 kg ITMs and ETMs whose diameter and thickness are 22 cm and 15 cm, respectively. The size is currently the largest in the market available for high-quality *c*-axis windows. *C*-axis is the optical axis of the sapphire which has no birefringence. The system design requires less than 100 ppm round trip loss in the cavities and low-absorption sapphire crystals to reach the target cryogenic temperature. Fabrication of such test mass mirrors was not straightforward and took time, but we have successfully obtained sapphire test mass mirrors which meet the requirement for bKAGRA. The details of the sapphire test masses will be explained elsewhere.

Other mirrors such as the beam splitter (BS), power recycling mirrors (PRM, PR2, PR3), signal recycling mirrors (SRM, SR2, SR3), and input/output mode matching telescope (IMMT/OMMT) mirrors are fused silica mirrors left at room temperature. The substrates of PR2, PR3,

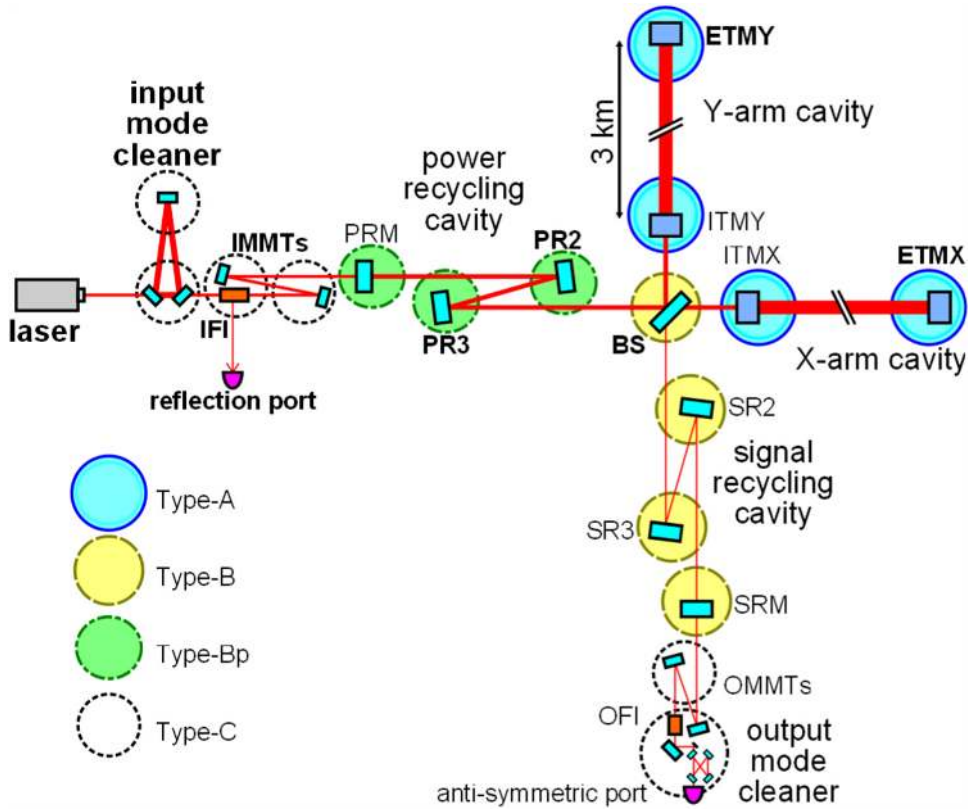


Figure 1. Schematic of the bKAGRA interferometer. All the mirrors shown are suspended inside the vacuum tanks with four types of vibration isolation systems. IMMT (OMMT): input (output) mode-matching telescope, IFI (OFI): input (output) Faraday isolator. Optics used in the Phase 1 operation are labeled in bold.

SR2 were formerly initial LIGO 25 cm-diameter test masses, and we resurfaced and coated them to match KAGRA's optical configuration. The substrates for the other room temperature mirrors were manufactured by a glass company in Japan, and polishing and coating have been completed as planned. Diameter of the beam splitter mirror, power/signal recycling mirrors, and input/output mode matching telescope mirrors are 37 cm, 25 cm, and 10 cm, respectively.

The arm cavities have a length of 3 km and a finesse of 1530. The finesse can be calculated with

$$\mathcal{F} = \frac{2\pi}{T_{\text{tot}}}, \quad (1)$$

where T_{tot} is the total optical loss of the optical cavity, and is related to the bandwidth of the cavity. The SRM is installed at the anti-symmetric port to extract the GW signal and thus broaden the detector bandwidth. In order to reduce the power inside the ITM substrate to reduce the heat absorption, KAGRA decided to use higher arm cavity finesse than Advanced LIGO and Advanced Virgo. This results in a narrower arm cavity bandwidth, and therefore employing RSE is more important than other detectors. There is an option to detune the signal recycling cavity length to further optimize the spectral shape of the quantum noise to increase

the binary neutron star inspiral range [7, 8]. Also, the power recycling technique is used to effectively increase the input power by a factor of 10.

The interferometer is also equipped with input and output mode cleaners (IMC and OMC). The IMC is a triangular ring cavity formed by three suspended mirrors, and has a round-trip length of 53.3 m and a finesse of 540. The IMC length is used as a frequency reference above ~ 1 Hz for pre-stabilization of the laser frequency. The OMC is a bow-tie cavity formed by four mirrors monolithically fixed on a base plate, and has a round-trip length of 1.5 m and a finesse of 780 [17]. The OMC rejects unwanted higher-order spatial modes and frequency sidebands, and the GW signal is extracted from the DC power of the OMC transmitted beam.

The interferometer is installed in the vacuum tanks at 10^{-7} Pa to mitigate noise from residual gasses. The interferometer mirrors are suspended by four different types of vibration isolation systems inside vacuum tanks, depending on their displacement noise requirements [18] (see figure 2). ITMs and ETMs are suspended by Type-A system which is an eight-stage pendulum suspended from a top geometric anti-spring (GAS) filter on an inverted pendulum table [19]. The GAS filters are for vertical vibration isolation, while the inverted pendulum table is for horizontal vibration isolation. The Type-A system extends over two stories and the legs of the inverted pendulum table are fixed on the second floor. From the top GAS filter, three standard GAS filters, a bottom GAS filter and a cryogenic payload [20] are suspended by a single maraging steel fiber in the order mentioned.

The cryogenic payload is the last four stages of the pendulum which are cooled down to cryogenic temperatures. The schematic of the cryogenic suspension system is shown in figure 3. The platform and marionette are suspended from the bottom filter and platform, respectively, with a single maraging steel wire. The intermediate mass is suspended from the marionette with four CuBe fibers. The test mass is in turn suspended from four sapphire blade springs attached to the intermediate mass, with four sapphire fibers (35 cm long, 1.6 mm in diameter). The heat deposited on to the test masses through optical absorption of the arm cavity beam is extracted via these sapphire fibers [21, 22]. The intermediate mass is cooled down to about 16 K via high purity 99.9999% (6N) aluminum heat links attached to the upper stages. The cryogenic payload is surrounded by 8 K inner shields and 80 K outer shields. The temperature of the inner shield is designed to be enough below the temperature of the cryopayload. This is because the heat introduced from the stray light could increase the temperature of the inner shield from the designed temperature.

The cryostat for the test masses also have various kinds of baffles for absorbing stray light inside the cavity, and duct shields at both sides for absorbing the room temperature thermal radiation from vacuum ducts [23, 24]. We use four low vibration double-stage pulse-tube cryocoolers for each cryostat [25, 26]. The outer shield of the cryostat is cooled down by the first stages of the four cryocooler units. The second stages of two cryocooler units cool the cryogenic payload and the other two cool the inner shield. We also use two single-stage cryocooler units to cool down the duct shields.

For room temperature mirrors, simpler vibration isolation systems are used. BS and signal recycling mirrors are each suspended by a Type-B system which is a four-stage pendulum suspended from a top geometric anti-spring filter on an inverted pendulum table, similar to Type-A [27]. The power recycling mirrors are each suspended from a triple pendulum called Type-Bp, which is a simplified version of Type-B [28]. Type-Bp system are not supported by an inverted pendulum table. It is instead supported by a set of motorized linear stages, called a traverser, for adjusting the position and the alignment of the suspension chain. The mirrors for the IMC and mode matching telescopes are each suspended from a double pendulum fixed on a three-stage stack for vibration isolation [29]. This system is called a Type-C system and is a modified version of the suspension used for the TAMA300 GW detector [30].

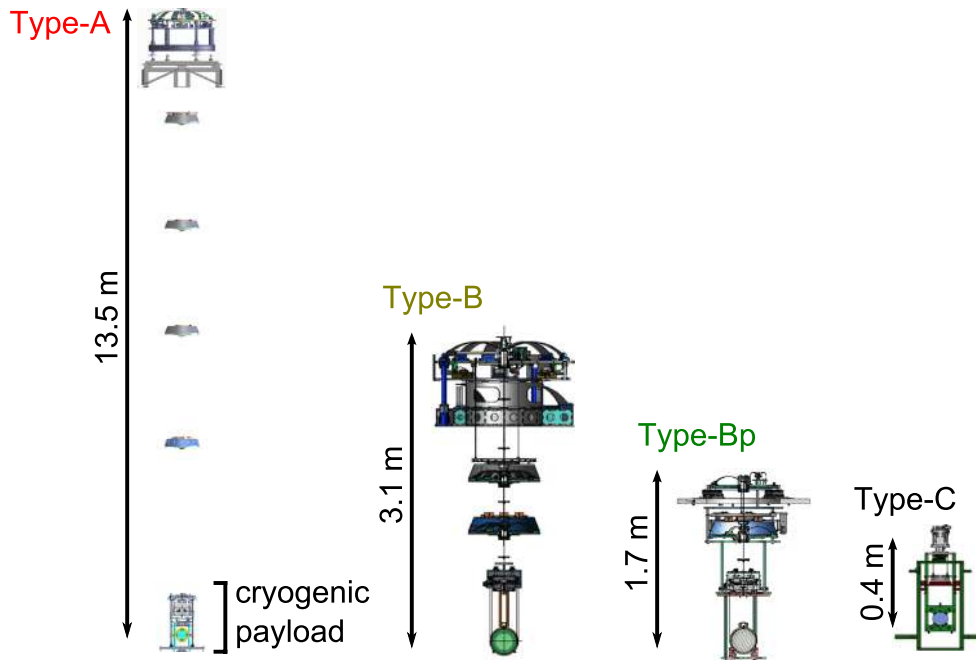


Figure 2. KAGRA mirror suspension system consists of four types. Type-A system is for ITMs and ETMs [19, 20]. Type-B system is for BS and signal recycling mirrors [27]. Type-Bp system is for power recycling mirrors [28]. Type-C system is used for other auxiliary mirrors [30]. Adapted from [28]. © IOP Publishing Ltd. All rights reserved.

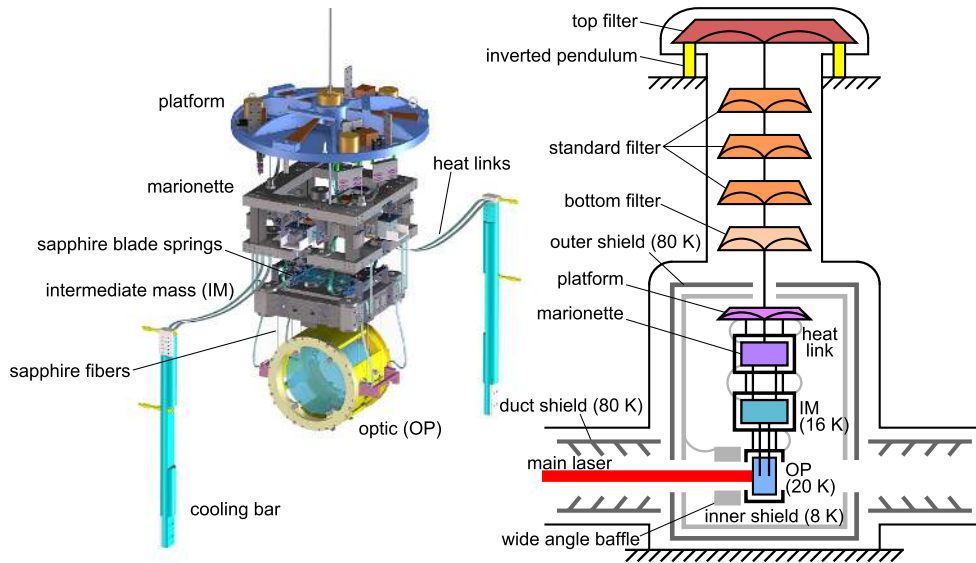


Figure 3. The CAD drawing of the cryogenic payload under Type-A (left) and the schematic of the cryogenic suspension system of sapphire test masses (right). Suspension stages outside of the outer shield are at room temperature.

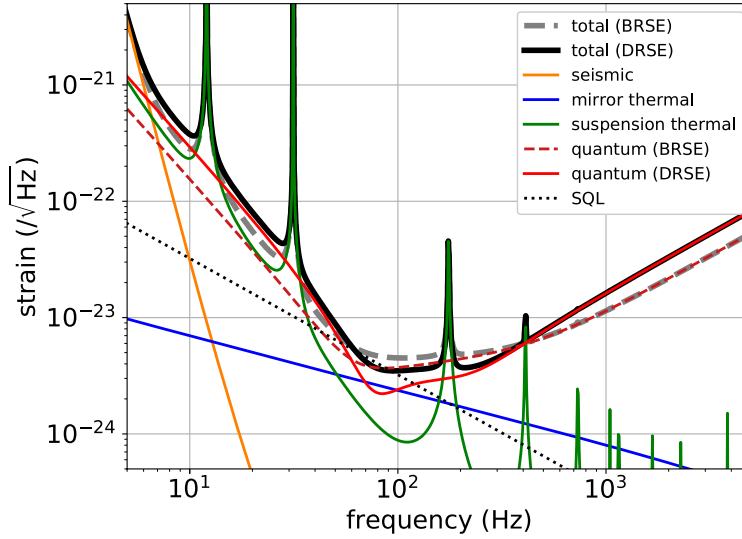


Figure 4. The designed sensitivity of bKAGRA. The quantum noise in both broadband and detuned RSE (BRSE and DRSE) cases are shown. The mirror thermal noise includes terms due to the test mass substrates and the coatings. The seismic noise includes the estimated Newtonian noise from the surface and bulk motion of the mountain containing KAGRA.

Figure 4 shows the designed sensitivity of bKAGRA. The quantum noise limits the sensitivity for almost the whole frequency band, but the suspension thermal noise and the coating thermal noise also contributes significantly below ~ 100 Hz. To reduce quantum shot noise, higher input power is preferred. However, because of the non-zero absorption of the sapphire mirrors, higher input power results in higher mirror temperature and therefore higher thermal noise. Taking these effects into account, the designed input power at PRM and mirror temperature were chosen to be 67W and 22 K, respectively, to maximize the binary neutron star inspiral range. The range reaches 135 Mpc in the broadband RSE configuration and 153 Mpc in the detuned RSE configuration with optimal homodyne readout angles. The details of the noise calculations and sensitivity design are described in [7, 31]. The main design parameters of bKAGRA is shown in table 3.

3. bKAGRA Phase 1 operation

In the Phase 1 operation, two ITMs and optics downstream of the signal recycling cavity were not installed. The PRM was installed but intentionally mis-aligned and we operated the interferometer as a 3 km Michelson interferometer configuration. The optics used in the Phase 1 operation are labeled in bold in figure 1. The GW signal was extracted from the interferometer reflected beam out of the input faraday isolator. We used a heterodyne readout employing modulation-demodulation technique at 16.87293 MHz. The phase modulation depth was measured to be 0.12 rad, and the input power at BS was at around 50 mW. The BS was used as an actuator for the length control of the Michelson interferometer with a control bandwidth of around 50 Hz. The measured interferometer visibility was 99%. The pressure inside the vacuum tanks varied from 10^{-5} Pa to 10^{-4} Pa along the 3 km arms.

Table 3. The main design parameters of bKAGRA. ITM and ETM have the same radius of curvature and beam radii incident on them. PRC: power recycling cavity, SRC: signal recycling cavity.

Arm cavity length	3000 m	Test mass size	$\phi 22 \text{ cm} \times 15 \text{ cm}$
Laser wavelength	1064 nm	Mass of test mass	22.8 kg
Input power at PRM	67 W	Test mass temperature	22 K
Arm intra-cavity power	340 kW	Beam radius at test masses	3.5 cm
Arm cavity finesse	1530	Test mass radius of curvature	1900 m
ITM transmittance	0.4%	PRC/SRC lengths	66.6 m/66.6 m
PRM transmittance	10%	Detuning angle	3.5 deg
SRM transmittance	15%	Homodyne angle	135.1 deg

The ETM for Y arm (ETMY) was suspended by a full cryogenic payload using a Type-A suspension, but the ETM for X arm (ETMX) was suspended by a cryogenic payload without heat links to investigate the effect on the vibration isolation system. The ETMY was cooled down to 18 K, and the ETMX was left at room temperature. One thing to be mentioned here is that a prototype ETMY mirror was used in Phase 1 operation since the high quality mirrors for bKAGRA were not quite ready. The main differences are figure errors in the coated surface and losses in the coating. Although its quality is not as good as the final one, the mirror functioned properly as mentioned in this paper.

Although the interferometer configuration was very simple, it was the first time that a km-scale interferometer with a sapphire mirror at a cryogenic temperature was operated. Also, it was the first time that all the types of KAGRA suspensions were employed. We also conducted various measurements on mirror installation accuracy, cryogenic cooling, suspensions, and interferometer stability.

3.1. Initial beam alignment and installation accuracy

Aligning the laser beam back and forth along the 3 km vacuum tubes requires the mirrors to be aligned to within a few tens of micro-radians. To aid the alignment process, we have installed four photodiodes in front of ETMs, around 10 cm away from the ETM high reflective surface. The four photodiodes are placed concentrically around the center of the ETM so that the readout gives the two-dimensional position of the beam with respect to the center of the ETM. Note that, in final configuration of KAGRA, these photodiodes will be placed on the baffle to capture narrow angle scattering, about 36 m away from the ETM [24].

We have also installed a telephoto camera (Tcam) system to monitor the position of the beam on the test mass high-reflective surface [32]. The Tcam system is similar to the system used to monitor the spot positions of the photon calibrator beams in Advanced LIGO [33]. We used a digital camera (Nikon D810) with a telescope (Sky-Watcher BKMAK127) to monitor the ETM surface 36 m away. The long focal distance was necessary to avoid conflict with the cryogenic duct shields and baffles. The camera image was updated at 1 Hz at maximum, and the spatial resolution was around 0.1 mm, which is small enough compared with the size of the beam (3.5 cm in $1/e^2$ radius). The Tcam system was also used to monitor the change in the position of the mirror during the cooling process, and to monitor the spot positions of the photon calibrator beams [34].

After the alignment of the beams to form a 3 km Michelson interferometer, we have conducted a series of experiments to measure the horizontal and vertical beam positions with

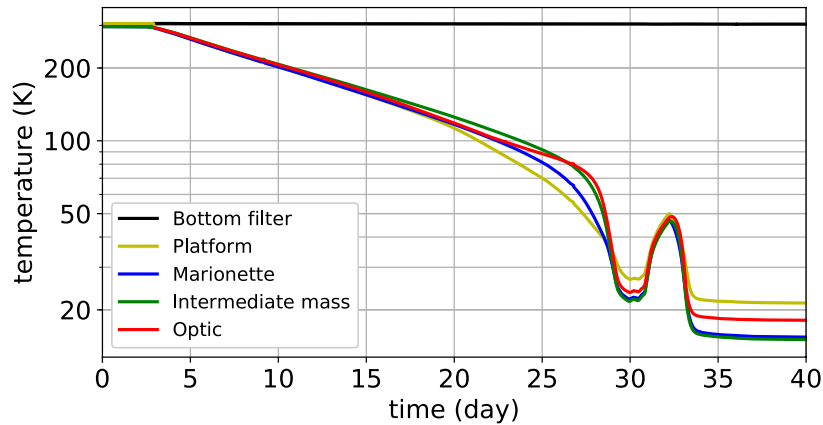


Figure 5. Cooling curve of ETMY. The bump starting from around day 30 was due to the restart of the cryocoolers.

respect to the center of the vacuum tubes or vacuum tanks. The discrepancies between the measured and designed positions stayed within 1 cm, which is reasonable considering the installation accuracy of the vacuum tanks. An accurate measurement of the 3-km arm length was not possible in Phase 1 operation, but we have measured the IMC length by measuring the free spectral range. The measured free spectral range was 5.624 308(1) MHz, which corresponds to a round-trip length of 53.300 30(1) m. The difference between the measured and designed length was 1.3 cm.

We therefore concluded that the mirror installation was done at an accuracy of about 1 cm. This is small enough compared with the position and alignment tuning range of the suspensions.

3.2. Cryogenic cooling of the sapphire mirror

The cryogenic cooling of ETMY started from the beginning of February 2018 and the temperature of the test mass reached below 20 K in about a month. Figure 5 shows the cooling curve of ETMY cryogenic payload for different suspension stages. Until around the 20th day, radiative cooling dominates the cooling process, but after that conduction cooling dominates and the cooling rate is increased [25]. Before reaching 20 K, one of the cryocoolers which cools down the cryogenic payload entered a quasi-stable state at 23 K due to an unbalance of the temperature distribution inside. We therefore stopped and restarted the four cryocoolers. Finally, the sapphire mirror reached 18 K and the intermediate mass reached 16 K. The cooling time and the temperatures reached are almost as expected. Details of the cryogenic system will be given in a separate paper [35].

During the cool down, the alignment of ETMY drifted hundreds of micro-radians, mainly in the yaw axis. Therefore, keeping the alignment of the Michelson interferometer continuously during the cool down was not possible. The restoration of the alignment was possible using the alignment actuators on the bottom filter and the marionette stages (see figure 3). These alignment actuators have a range of ± 18 mrad for yaw, and ± 24 mrad for pitch. The height change of the test mass due to shrinking of the sapphire fibers and the spring constant change in the blade springs from the cooling is estimated to be around 1 mm and 0.1 mm,

respectively. Since pitch drift was around $100 \mu\text{rad}$, we confirmed that variation in the shrinking between different fibers were less than 1%.

3.3. Characterization of suspensions

To operate interferometric GW detectors with high sensitivity, the relative positions and alignments of the mirrors must be finely tuned to maintain the interference conditions. For this purpose, mirror suspension systems are equipped with actuators at various suspension stages. In KAGRA, actuators used for the interferometer length control and alignment control consist of coils and magnets, and actuation is done by controlling the current applied to the coils. Details of the mirror actuation design can be found in [18].

The performance of the mirror actuation system, especially its performance under cryogenic temperatures, is therefore a critical part of the KAGRA interferometer. During Phase 1, we measured the transfer functions from voltage applied to the coil drivers to the displacement of the mirror using the Michelson interferometer as a displacement sensor, to check the performance. Figure 6 shows the result of the measurement, compared with expected curves from suspension models described in [18]. In the suspension model, the transfer functions from the actuator force applied to each suspension stage to the displacement of the mirror are calculated using a suspension rigid-body simulation tool, called SUMCON [36]. The coil-magnet actuation efficiencies in the unit of N/A used in the model are the values measured as a standalone actuator.

The measured transfer function matched with the model within a factor of two for BS and ETMX at room temperature. For ETMY at cryogenic temperatures, spurious couplings were found, especially in the marionette. These spurious couplings could be caused by electronics cables from the cryogenic payload to upper stages touching the walls of the vacuum tank. We also found that three standard GAS filters for ETMY were not working properly since some of the parts were mechanically touching the frame. ETMY was the first full Type-A suspension system installed. An improved mechanism for the height adjustment and the installation procedure were employed in ETMX suspension to avoid the same issues. We did not find such issues for ETMX.

Comparison of the ETMX and ETMY actuator transfer function measurements gives the coil-magnet efficiency difference between room and cryogenic temperatures. The coil-magnet efficiency at 20 K calculated from the ETMY transfer function measurements was around 30% higher than that at room temperature, calculated from ETMX measurements. We note that the coil drivers used for Phase 1 operation was different from the default ones described in [18]. Except for ETMX optics stage which used the low power and low noise coil driver, high power but higher noise coil drivers are used for BS, ETMX and ETMY suspensions to give a larger actuation range.

3.4. Interferometer control and calibration

The block diagram of the Michelson interferometer control in Phase 1 operation is shown in figure 7. The differential arm length change caused by mirror displacements is measured with the fringe of the Michelson interferometer. The signal from the photodiode detecting the fringe is sent to the KAGRA digital system via 16-bit analog-to-digital converter (ADC) with a range of $\pm 20\text{V}$. The digital system generates the feedback signal with infinite impulse response servo filters, and the feedback signal are sent to coil drivers via 16-bit digital-to-analog converter (DAC) with a range of $\pm 10\text{V}$. We used both the optic and the intermediate mass

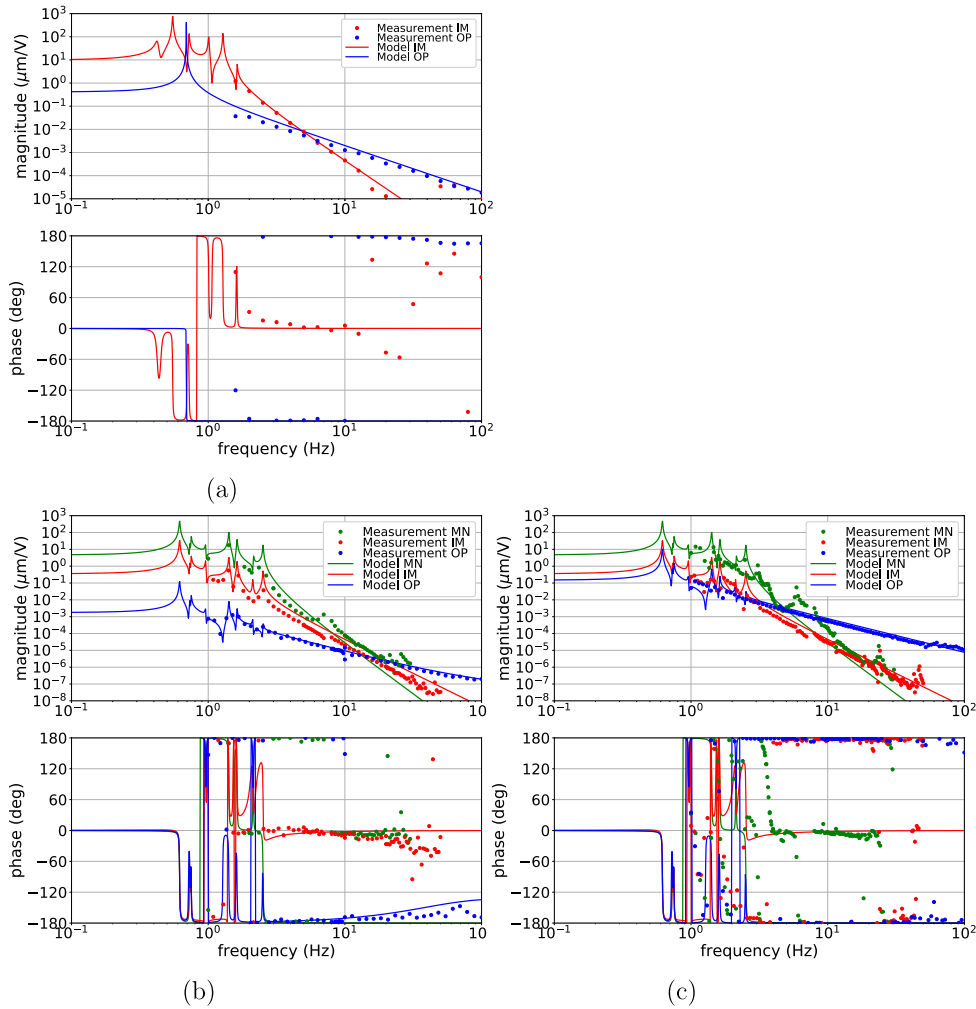


Figure 6. Actuation transfer functions of BS (top left), ETMX (bottom left) and ETMY (bottom right). The transfer functions from the voltage applied to the coil drivers to the optic displacements are shown. The measurement results and expected curves from suspension models described in [18] are plotted for marionette (MN), intermediate mass (IM) and optic (OP) stages. (a) BS. (b) ETMX. (c) ETMY.

stages of BS for the actuation, with a crossover frequency at around 0.4 Hz. Below the crossover frequency, the intermediate mass stage was mainly used. ADCs and DACs operate at a sampling frequency of 65 536 Hz and has a total timing delay of $14.6 \mu\text{s}$. The sampled signals are down-converted to 16 384 Hz by the digital system. We used analog 3rd-order Butterworth low-pass filters with a cut-off frequency of 10 kHz for anti-aliasing and anti-imaging. For down-sampling and up-sampling in the digital system, we used elliptic low-pass filters. These anti-aliasing and anti-imaging filters each has a timing delay of $47 \mu\text{s}$. We used a whitening filter with a zero at 1 Hz and a pole at 10 Hz to effectively reduce the ADC noise.

The calibration of the mirror displacement was done using the fringe of the Michelson interferometer when the mirror is freely swinging. The calibration factor from the mirror displacement to the error signal, which we call optical gain, was typically measured to be

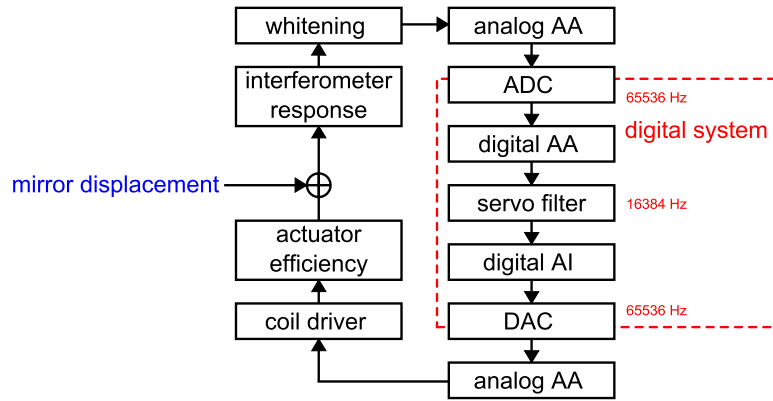


Figure 7. Block diagram of the Michelson interferometer control in Phase 1 operation. AA: anti-aliasing filter, AI: anti-imaging filter.

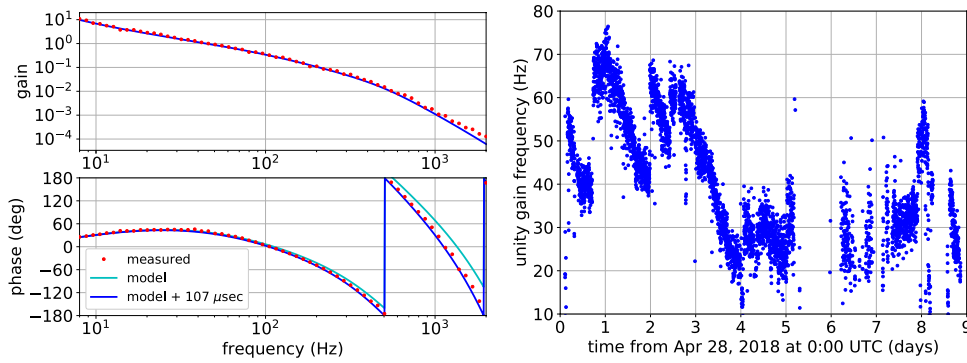


Figure 8. The openloop transfer function of the Michelson interferometer control (left) and estimated unity gain frequency over time (right). The expected openloop transfer function matches with the measurement by adding $107 \mu\text{s}$ extra phase delay.

$(5.7 \pm 0.7) \times 10^7 \text{ V m}^{-1}$. The uncertainty mainly comes from the fluctuation of the interferometer fringe from alignment fluctuations of the mirrors.

The measured openloop transfer function of the servo is shown left in figure 8. The unity gain frequency of the servo was typically at 50 Hz. To monitor the openloop transfer function change over time, we have injected three calibration lines, at 15 Hz, 51 Hz, and 91 Hz, using BS. The unity gain frequency drift calculated from the calibration line at 91 Hz is shown right in figure 8. The overall gain drifted by about 50% per an hour. Although it is generally not possible to distinguish what is the cause of this drift, we have occasionally measured the optical gain and actuator efficiency during the operation when the interferometer is not locked, and concluded that it is likely to be from the optical gain drift. The optical gain drift was caused by visibility degradation from the Michelson interferometer alignment drift. This was also the case in iKAGRA operation.

From the openloop transfer function measurement, we have also measured the overall timing delay of the loop. The measured delay was $520 \pm 3 \mu\text{s}$, and we had an unexpected delay of about $107 \mu\text{s}$. Our model accounts for all the timing delays mentioned above and the time it takes for transferring signals between separated digital control computers ($168 \mu\text{s}$), giving a

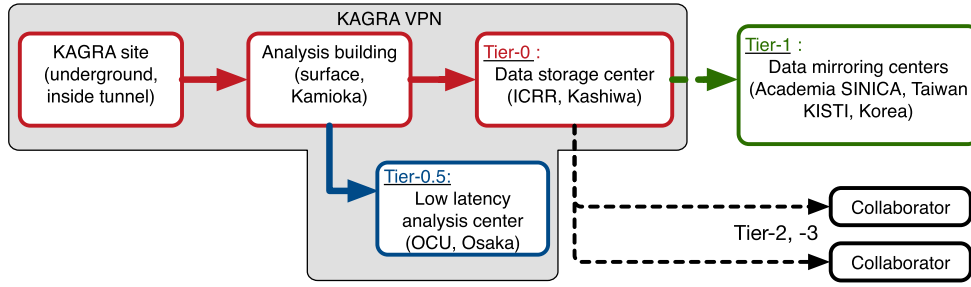


Figure 9. Overview of the KAGRA data transfer system. Tier-0 (original) and Tier-0.5 (low latency) are formed as isolated local network using VPN (virtual private network).

total of $413 \mu\text{s}$. We suspect that the cause of the unexpected time delay comes from the delays in the digital control system and electronics we have not taken into account in the model. Timing delay measurements on each component are underway.

The input and output of the servo filter in the digital system are called the error signal v_{err} and the feedback signal v_{fb} , respectively. Using these signals, we have reconstructed the Michelson differential arm length change in the frequency domain with

$$\delta L = \frac{1}{C} v_{\text{err}} + A v_{\text{fb}}, \quad (2)$$

where C is the optical gain and A is the actuation efficiency. The reconstruction was done online using infinite impulse response filters, and the latency was less than 1 s.

3.5. Data transfer

The acquired KAGRA interferometer signals, some channels inside the digital control servo loop and other monitor channels are recorded into frame format files in 32 s chunks and are transferred to multiple data centers as shown in figure 9. The frame format is an international common data format of GW experiments [39]. All the raw data from the KAGRA detector inside the tunnel is first transferred to a control room in the analysis building on the ground via 4.5 km optical fiber links. The total data rate is expected to reach 20 MB s^{-1} in the final phase of bKAGRA. The analysis building has a 200 TB data storage system which can store about four months of data. The raw data and processed data including calibrated strain signal $h(t)$ are then transferred to the data storage center at the Institute for Cosmic Ray Research in Kashiwa and the low latency data analysis center at Osaka City University. The data storage center has a storage system with a capacity of 2.5 PB. The low latency data analysis center has 760 CPU cores. We also transfer the data to data mirroring centers in Taiwan and Korea. The strain signal data can be exchanged with other GW detectors such as LIGO and Virgo in future observational operations.

During Phase 1, we also tested the data transfer system for various use cases: analysis of hardware injected waveforms, development of event search pipe-lines, detector characterization, and test of the data transfer system itself, etc. The measured data transfer speed from the KAGRA detector to the analysis building was about 200 MB s^{-1} , which exceeds the requirement of 20 MB s^{-1} . The measured latencies of the data transfer from the KAGRA site to the low latency analysis site in Osaka was about 3 s.

We have been developing data analysis tools at the data storage center in Kashiwa. Daily spectra of the major channels are generated automatically and served via a web page to the

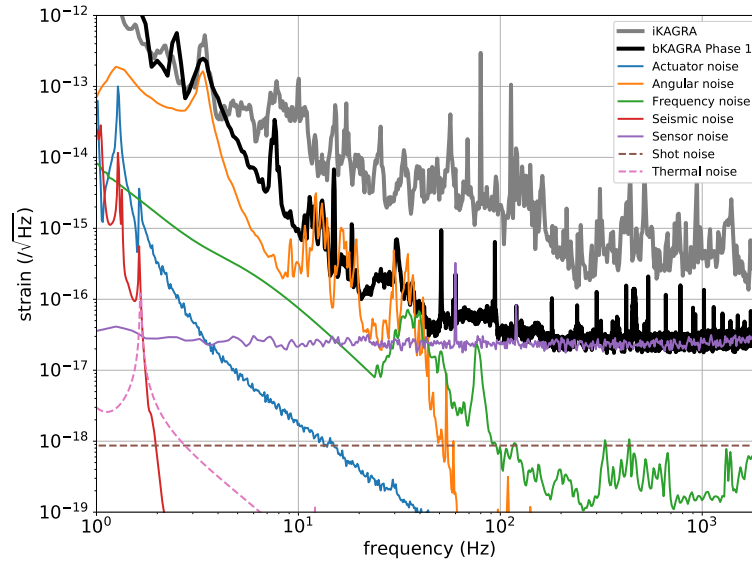


Figure 10. The strain sensitivity of KAGRA during Phase 1 operation, compared with various strain equivalent noises. Actuator noise is the sum of the displacement noise of the mirrors from electronics noise for the actuation [18]. Angular noise is the sum of the mirror angular fluctuation coupled to the displacement signal. Frequency noise is the estimated laser frequency noise suppressed through laser frequency stabilization using IMC. Seismic noise is estimated mirror displacement noise from the ground displacement attenuated by the mirror suspensions. Sensor noise is the sum of ADC noise and the dark noise of the photodiode. Thermal noise is the estimated suspension thermal noise of ETMX. That for ETMY is smaller by more than an order of magnitude due to cooling. The peaks at 80 Hz and 113 Hz for iKAGRA, and those at 15 Hz, 51 Hz and 91 Hz for Phase 1 are from the calibration lines.

collaborators. To realize very low latency off-line searches, data from the frame file is transmitted to multiple servers with shared memory dedicated to these calculations. We have also implemented a matched filtering analysis for compact binary coalescences.

3.6. Interferometer sensitivity and stability

Although Phase 1 was not meant for low noise operation to detect GWs, we have also checked the strain sensitivity of the detector. A typical sensitivity curve during the Phase 1 operation is shown in figure 10. Below around 50 Hz, the sensitivity was limited by angular control noise, mainly from BS motion in yaw. During Phase 1, angular motions of PR2, BS, ETMX and ETMY are controlled using optical levers as angular sensors [38]. Above 100 Hz, the sensitivity was limited by the dark noise of the photodiodes receiving an error signal for the Michelson interferometer length control. The dark noise was quite high since the photodiodes used are optimized for the full power operation of bKAGRA. Compared with iKAGRA, sensitivity was improved by more than an order of magnitude mainly due to reduced acoustic noise coupling. In iKAGRA, acoustic noise was high because vacuum chambers were not evacuated [15].

Figure 11 shows the daily duty factor, inspiral range, and root-mean-square of the seismometer output. The inspiral range for binary neutron stars was about 17 pc and that for $30M_{\odot}$ – $30M_{\odot}$ binary black holes was about 100 pc. The overall duty factor, the ratio of the locked

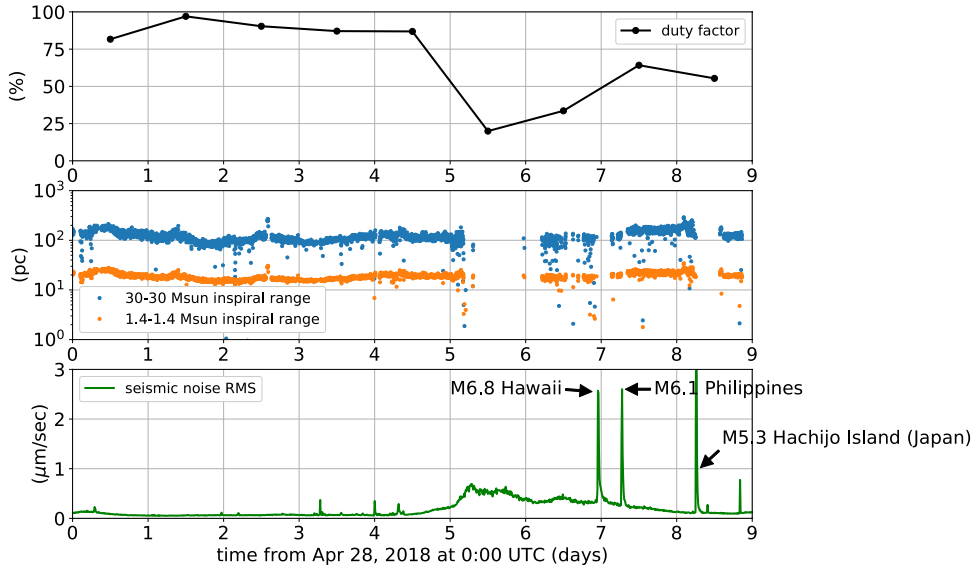


Figure 11. Daily duty factor (top), inspiral range (middle), and seismic noise level (bottom) during Phase 1 operation. The root-mean-square (RMS) of the ground velocity measured with a seismometer is shown.

period to the whole operation period, was 69%. The micro-seismic noise was higher at the last half of the operation due to local stormy weather, and the interferometer was not stable. As we have discussed in [15], the micro-seismic level could vary for more than an order of magnitude depending on weather conditions. In April to May in 2018, high micro-seismic motion was observed roughly once per 1–2 weeks, and high micro-seismic motion we have observed during the Phase 1 operation was not unusual. Also, big earthquakes in Hawaii, Philippines, and Hachijo Island of Japan affected the interferometer. According to the United States Geological Survey, their magnitude was 6.8, 6.1 and 5.3, respectively. The effect of seismic motion was higher than expected due to rubbing issues in the ETMY suspension, as discussed in section 3.3.

The duty factor during the first half of the operation when the seismic noise was lower reached 88.6%. The lock of the interferometer was done automatically using a state machine automaton called *Guardian* [37]. The recovery of the lock often took less than 10 min from lock loss. The longest stretch in which lock was maintained was 11.1 h, which was achieved in May 3.

4. Conclusions and outlook

We have operated a 3 km Michelson interferometer with a cryogenic sapphire mirror for the first time. The sapphire mirror was suspended by a full eight-stage pendulum, and was successfully cooled down to below 20 K within 35 d. The alignment drift during the cool down and mirror actuation efficiency were measured, and we confirmed that interferometer alignment and control is possible at cryogenic temperatures. We have also checked the mirror installation accuracy, and confirmed that the accuracy is good enough to form a full interferometer. There were some issues regarding rubbing of electric cables and stuck GAS filters in

the first test mass suspension system installed, but these issues were successfully resolved in the second system.

The Phase 1 operation marked the first step in realizing a full 3 km cryogenic interferometer at an underground site. After the Phase 1 operation, we have been installing more mirror suspension systems and a higher power laser source to form a full RSE interferometer at cryogenic temperatures. The prototype ETMY was replaced with the final ETMY mirror, and the rubbing issue of electric cables was resolved by improved cabling procedure. The issue regarding stuck GAS filters are planned to be fixed in the future since the degradation in the vibration isolation performance has a small impact on the sensitivity in the first observation runs. We expect to finish all installation work by the end of March 2019⁷⁹, and start commissioning of the detector then. The first scientific observation run shall be started in late 2019.

Acknowledgments



We would like to thank the Advanced Technology Center (ATC) of NAOJ, the Mechanical Engineering Center of KEK, and the machine shop of the Institute of Solid State Physics (ISSP) of the University of Tokyo for technical support.

This work was supported by MEXT, JSPS Leading-edge Research Infrastructure Program, JSPS Grant-in-Aid for Specially Promoted Research 26000005, JSPS Grant-in-Aid for Scientific Research on Innovative Areas 2905: JP17H06358, JP17H06361 and JP17H06364, JSPS Core-to-Core Program A. Advanced Research Networks, JSPS Grant-in-Aid for Scientific Research (S) 17H06133, the joint research program of the Institute for Cosmic Ray Research, University of Tokyo, National Research Foundation (NRF) and Computing Infrastructure Project of KISTI-GSDC in Korea, Academia Sinica (AS), AS Grid Center (ASGC) and the Ministry of Science and Technology (MoST) in Taiwan under grants including AS-CDA-105-M06, the LIGO project, and the Virgo project. This paper carries JGW Document Number JGW-P1809289.

ORCID iDs

T Akutsu  <https://orcid.org/0000-0003-0733-7530>
A Araya  <https://orcid.org/0000-0002-6884-2875>
S Bae  <https://orcid.org/0000-0003-2429-3357>
E Capocasa  <https://orcid.org/0000-0003-3762-6958>
T-W Chiu  <https://orcid.org/0000-0002-7371-1132>
N Kanda  <https://orcid.org/0000-0001-6291-0227>
C Kim  <https://orcid.org/0000-0003-3040-8456>
A K H Kong  <https://orcid.org/0000-0002-5105-344X>
H M Lee  <https://orcid.org/0000-0003-4412-7161>
H W Lee  <https://orcid.org/0000-0002-1998-3209>
C-Y Lin  <https://orcid.org/0000-0002-7489-7418>
Y Michimura  <https://orcid.org/0000-0002-2218-4002>
K Nakamura  <https://orcid.org/0000-0001-6148-4289>
H Nakano  <https://orcid.org/0000-0001-7665-0796>
L Nguyen Quynh  <https://orcid.org/0000-0002-1828-3702>
J J Oh  <https://orcid.org/0000-0001-5417-862X>

⁷⁹We have actually finished all the planned installations for the first observation run in the middle of April 2019.

J Park  <https://orcid.org/0000-0002-7510-0079>
 H Shinkai  <https://orcid.org/0000-0003-1082-2844>
 A Shoda  <https://orcid.org/0000-0002-0236-4735>
 E J Son  <https://orcid.org/0000-0002-9234-362X>
 S Tanioka  <https://orcid.org/0000-0003-3321-1018>
 F Travasso  <https://orcid.org/0000-0002-4653-6156>
 T Uehara  <https://orcid.org/0000-0003-4375-098X>
 H Vocca  <https://orcid.org/0000-0002-1200-3917>
 K Yamamoto  <https://orcid.org/0000-0002-5064-4619>
 T Yamamoto  <https://orcid.org/0000-0002-0808-4822>
 Z-H Zhu  <https://orcid.org/0000-0002-3567-6743>

References

- [1] Abbott B P *et al* (LIGO Scientific Collaboration and Virgo Collaboration) 2016 *Phys. Rev. Lett.* **116** 061102
- [2] Abbot B P *et al* (The LIGO Scientific Collaboration and The Virgo Collaboration) 2018 (arXiv:1811.12907)
- [3] Abbott B P *et al* (LIGO Scientific Collaboration and Virgo Collaboration) 2017 *Phys. Rev. Lett.* **119** 161101
- [4] www.gw-openscience.org/catalog/
- [5] Aasi J *et al* (The LIGO Scientific Collaboration) 2015 *Class. Quantum Grav.* **32** 074001
- [6] Acernese F *et al* (Virgo Collaboration) 2015 *Class. Quantum Grav.* **32** 024001
- [7] Somiya K and KAGRA Collaboration 2012 *Class. Quantum Grav.* **29** 124007
- [8] Aso Y, Michimura Y, Somiya K, Ando M, Miyakawa O, Sekiguchi T, Tatsumi D and Yamamoto H and The KAGRA Collaboration 2013 *Phys. Rev. D* **88** 043007
- [9] KAGRA Collaboration 2019 *Nat. Astron.* **3** 35
- [10] Punturo M *et al* 2010 *Class. Quantum Grav.* **27** 194002
- [11] Abbott B P *et al* (LIGO Scientific Collaboration) 2017 *Class. Quantum Grav.* **34** 044001
- [12] Abbott B P *et al* (KAGRA Collaboration, LIGO Scientific Collaboration and Virgo Collaboration) 2018 *Living Rev. Relativ.* **21** 3
- [13] Takeda H, Nishizawa A, Michimura Y, Nagano K, Komori K, Ando M and Hayama K 2018 *Phys. Rev. D* **98** 022008
- [14] Hagihara Y, Era N, Iikawa D and Asada H 2018 *Phys. Rev. D* **98** 064035
- [15] Akutsu T *et al* (KAGRA Collaboration) 2018 *Prog. Theor. Exp. Phys.* **2018** 013F01
- [16] Hirose E, Bajuk D, Billingsley G, Kajita T, Kestner B, Mio N, Ohashi M, Reichman B, Yamamoto H and Zhang L 2014 *Phys. Rev. D* **89** 062003
- [17] Yano K, Kumeta A and Somiya K 2016 *J. Phys.: Conf. Ser.* **716** 012032
- [18] Michimura Y *et al* 2017 *Class. Quantum Grav.* **34** 225001
- [19] Hirose E, Sekiguchi T, Kumar R, Takahashi R and For the KAGRA Collaboration 2014 *Class. Quantum Grav.* **31** 224004
- [20] Kumar R, Chen D, Hagiwara A, Kajita T, Miyamoto T, Suzuki T, Sakakibara Y, Tanaka H, Yamamoto K and Tomaru T 2016 *J. Phys.: Conf. Ser.* **716** 012017
- [21] Khalaidovski A *et al* 2014 *Class. Quantum Grav.* **31** 105004
- [22] Komori K, Enomoto Y, Takeda H, Michimura Y, Somiya K, Ando M and Ballmer S W 2018 *Phys. Rev. D* **97** 102001
- [23] Sakakibara Y, Kimura N, Akutsu T, Suzuki T and Kuroda K 2015 *Class. Quantum Grav.* **32** 155011
- [24] Akutsu T *et al* 2016 *Opt. Mater. Express* **6** 1613
- [25] Sakakibara Y *et al* 2014 *Class. Quantum Grav.* **31** 224003
- [26] Chen D *et al* 2014 *Class. Quantum Grav.* **31** 224001
- [27] Peña Arellano F E *et al* 2016 *Rev. Sci. Instrum.* **87** 034501
- [28] KAGRA Collaboration 2019 *Class. Quantum Grav.* **36** 095015
- [29] Takahashi R *et al* 2002 *Rev. Sci. Instrum.* **73** 2428
- [30] Takahashi R and Arai K and The TAMA Collaboration 2002 *Class. Quantum Grav.* **19** 1599

- [31] Michimura Y, Komori K, Nishizawa A, Takeda H, Nagano K, Enomoto Y, Hayama K, Somiya K and Ando M 2018 *Phys. Rev. D* **97** 122003
- [32] Yokozawa T *et al* 2019 (in preparation)
- [33] Karki S *et al* 2016 *Rev. Sci. Instrum.* **87** 114503
- [34] Inoue Y, Haino S, Kanda N, Ogawa Y, Suzuki T, Tomaru T, Yamanmoto T and Yokozawa T 2018 *Phys. Rev. D* **98** 022005
- [35] Ushiba T *et al* 2019 (in preparation)
- [36] SUMCON (available from <https://gwdoc.icrr.u-tokyo.ac.jp/cgi-bin/DocDB/ShowDocument? docid=3729>)
- [37] Rollins J G 2016 *Rev. Sci. Instrum.* **87** 094502
- [38] Kokeyama K *et al* 2018 *Phys. Lett. A* **382** 1950
- [39] The Frame Library <http://lappweb.in2p3.fr/virgo/FrameL/>